Applied Catalysis B: Environmental 150–151 (2014) 564–573

Contents lists available at ScienceDirect

Applied Catalysis B: Environmental

journal homepage: www.elsevier.com/locate/apcatb

Study on the separation mechanisms of photogenerated electrons and holes for composite photocatalysts g-C_3N_4-WO_3

Shifu Chen [a,b,*], Yingfei Hu [b], Sugang Meng [b], Xianliang Fu [b]

[a] Department of Chemistry, Anhui Science and Technology University, Anhui, Fengyang, 233100, People's Republic of China
[b] Department of Chemistry, Huaibei Normal University, Anhui, Huaibei 235000, People's Republic of China

ARTICLE INFO

Article history:
Received 28 September 2013
Received in revised form
28 December 2013
Accepted 30 December 2013
Available online 7 January 2014

Keywords:
Composite photocatalyst
g-C_3N_4-WO_3
Photoexcited carriers
Transport process
Reaction mechanisms

ABSTRACT

The separation mechanisms of photogenerated electrons and holes for composite photocatalysts have been a research focus. In this paper, the composite g-C_3N_4-WO_3 photocatalysts with different main parts of C_3N_4 or WO_3 were prepared by ball milling and heat treatment methods. The photocatalytic performance was evaluated by degradation of methylene blue (MB) and fuchsin (BF) under visible light illumination. The photocatalyst was characterized by X-ray powder diffraction (XRD), UV–vis diffuse reflection spectroscopy (DRS), transmission electron microscopy (TEM) and Brunauer–Emmett–Teller (BET) methods. The separation mechanisms of photogenerated electrons and holes of the g-C_3N_4-WO_3 photocatalysts were investigated by electron spin resonance technology (ESR), photoluminescence technique (PL), and determination of reactive species in the photocatalytic reactions. When the main part of the g-C_3N_4-WO_3 photocatalyst is WO_3 (namely g-C_3N_4/WO_3), the transport process of the photogenerated electrons and holes adopts the generic band–band transfer. Meanwhile, g-C_3N_4 is covered by WO_3 powder, and the role of g-C_3N_4 can not be played fully. The photocatalytic activity of the photocatalyst is not obviously increased. However, when the primary part of the WO_3-g-C_3N_4 photocatalyst is g-C_3N_4 (namely WO_3/g-C_3N_4), the migration of photogenerated electrons and holes exhibits a typical characteristic of Z-scheme photocatalyst, and the photocatalytic activity of the photocatalyst is increased greatly.

1. Introduction

As photocatalysis can be applied to waste water treatment, environmental cleaning, and producing hydrogen from water splitting, it has been attracting much attention in recent years [1–3]. In order to achieve the above goals, two problems must be resolved, i.e., increasing the separation efficiency of photoexcited electron-hole pairs and extending the excitation wavelength range of photocatalysts [4,5]. To increase the absorption wavelength range, the semiconductor materials, such as oxides, sulfides, nitrides, and solid solutions etc., which can be excited by visible light, have been investigated extensively [6–9]. However, a single-phase photocatalyst exhibits significant limitations in the process of photocatalytic reactions due to the quick combination of photogenerated electrons and holes. To enhance the separation efficiency of photoexcited electron-hole pairs, the heterojunction composite photocatalysts have been fabricated extensively [10–13]. In general, when two semiconductors with the matching of band gap were coupled into a heterojunction photocatalyst, the photoexcited carriers are transferred into valence band (VB) and conduction band (CB) of opposite semiconductor respectively due to their potential difference of VB and CB [14–16]. However, the oxidation and reduction ability of the transferred photoexcited carriers are lower than that of original photoexcited carriers because of the difference of band positions. So exploitation of semiconductor photocatalysts with simultaneous high photooxidation and photoreduction performance is always a hot topic. Recently, the Z-scheme principle of photocatalyst has become a focus of research because of its stronger oxidation and reduction capability and higher photocatalytic performance than the single component. For example, a plasmonic Z-scheme visible-light photocatalyst $H_2WO_4{\cdot}H_2O$/Ag/AgCl exhibits a much higher photocatalytic activity than the one-component or two-component photocatalysts [17]. ZnO/CdS Z-scheme photocatalyst prolongs the lifetime of photoexcited carriers [18], and increases the photocatalyst activity.

Recently, a polymer photocatalyst named graphitic carbon nitride (g-C_3N_4) has attracted intensive attention for hydrogen and oxygen evolution via water splitting, photocatalytic degradation of organic pollutants, and photosynthesis under visible light illumination [19–21]. It is known that the band gap of g-C_3N_4 is about 2.7 eV, which can absorb visible light up to 460 nm. Furthermore, the CB

* Corresponding author at: Corresponding author. Tel.: +86 561 3806611; fax: +86 561 3090518.
E-mail address: chshifu@chnu.edu.cn (S. Chen).

0926-3373/$ – see front matter © 2014 Elsevier B.V. All rights reserved.
http://dx.doi.org/10.1016/j.apcatb.2013.12.053

minimum (−1.12 eV vs. NHE) of g-C_3N_4 is extremely negative, so photogenerated electrons should have high reduction ability. However, the photocatalytic efficiency of single g-C_3N_4 is limited due to the high recombination probability of photoexcited electron-hole pairs. In order to improve photocatalytic activity, many strategies such as doping and coupling g-C_3N_4 with other semiconductor materials or metal and nonmetal have been used to modify g-C_3N_4 [22–26].

Tungsten oxide (WO_3) is regarded as a promising material because of its special photocatalytic and electrochromic properties [27–30]. Compared with TiO_2, WO_3 has a smaller optical band gap (2.7 eV), and the VB position of WO_3 is extremely close to that of TiO_2. Therefore, the hole generated on the VB of WO_3 has a similar oxidative capability to that of TiO_2. However, the CB level of WO_3 is more positive than that of TiO_2, which results in the electron generated on the CB of WO_3 with a limited reductive ability than of TiO_2.

When WO_3 is combined with g-C_3N_4, a g-C_3N_4/WO_3 heterojunction photocatalyst may be formed between WO_3 and g-C_3N_4. The transfer of the photoexcited carriers of g-C_3N_4 and WO_3 will happen because of the position differences of VB and CB. There are two ways for the transfer of the photoexcited carriers. One is band–band transfer, and the other is Z-scheme principle transfer. It is known that the VB position of g-C_3N_4 is about 1.57 eV, and the CB position of WO_3 is about 0.74 eV [21,29]. Because of the short distance between the VB of g-C_3N_4 and the CB of WO_3, a Z-scheme system photocatalyst may be formed. If so, the holes generated on the VB of g-C_3N_4 are easily combined with the electrons generated on the CB of WO_3. Consequently, the photogenerated electrons on the CB of g-C_3N_4 exhibit strong reduction ability, and the photogenerated holes on the VB of WO_3 show excellent oxidation ability. However, to the best of our knowledge, there has been no report on the investigation of g-C_3N_4-WO_3 photocatalyst. Especially, the separation mechanisms of photoexcited carriers for the heterojunction photocatalysts have not been investigated extensively.

In this paper, different ratios of g-C_3N_4-WO_3 photocatalysts were prepared with ball milling and heat treatment methods. The photocatalytic activity was evaluated by degradation of methylene blue and fuchsin under visible light illumination. The g-C_3N_4-WO_3 photocatalysts were characterized in detail. The separation mechanisms of photogenerated electrons and holes of the g-C_3N_4-WO_3 photocatalysts were investigated by electron spin resonance technology, photoluminescence technique, and determination of reactive species in the photocatalytic reactions. Some interesting results were obtained. The separation mechanisms of photoexcited carriers for the composite photocatalysts were proposed.

2. Experimental

2.1. Materials

Melamine powder (Pur. >99.0%) used in the experiments was supplied by Aladdin Chemistry Co. Ltd. Ammonium tungstate hydrate was supplied by Sinopharm Chemical Reagent Co. Ltd. MB, BF, and other chemicals used in the experiments were purchased from Shanghai and other China chemical reagent Ltd. They are of analytically pure grade and used without further purification. Deionized water was used throughout this study.

2.2. Preparation of samples

g-C_3N_4 powder was prepared via heating melamine in a tube furnace. A certain amount of melamine was put into an alumina crucible which was first heated at 500 °C for 2 h and was further heated at 520 °C for 2 h with a temperature rise rate of 10 °C/min. After the reaction, the alumina crucible was cooled naturally to room temperature. The as-prepared g-C_3N_4 was collected and ground into powder. Pure WO_3 powder was prepared by the same heat treatment method using ammonium tungstate hydrate as a precursor.

The g-C_3N_4-WO_3 composite photocatalyst was fabricated as follows: The mixtures of melamine and ammonium tungstate hydrate with a certain ratio were added into a zirconia tank. Two different sizes of zirconia balls were mixed in the zirconia tank, and water was used as a dispersant. The mixed samples were ball milled for 1 h at the speed of 400 rpm, and then the wet powder was dried at 60 °C in air. The obtained powders were heated at the temperatures of 500 °C and 520 °C for 2 h, respectively. In this way, different WO_3(wt.%)/g-C_3N_4 photocatalysts (wt. = 0, 1.0, 3.0, 5.0, 7.0, 10, 30, 50, 70, 90, 93, 95, 97, 99, 100) were obtained, respectively. For convenience, when wt. < 10, i.e., the main part of the photocatalyst is g-C_3N_4, it is written as WO_3/g-C_3N_4; when wt. > 90, i.e., the main part is WO_3, it is written as g-C_3N_4/WO_3.

2.3. Photoreaction apparatus and procedure

Experiments were carried out in a photoreaction apparatus. The photoreaction apparatus consists of two parts [31,32]. The first part is an annular quartz tube. A 500 W Xenon lamp (Institute of Electric Light Source, Beijing) with a maximum emission at about 470 nm was used as visible light source. The wavelength of the visible light was controlled through a 400 nm cutoff filter ($\lambda > 400$ nm, Instrument Company of Nantong, China). The lamp is laid in the empty chamber of the annular tube, and running water passes through an inner thimble of the annular tube. Owing to continuous cooling, the temperature of the reaction solution is maintained at approximately 30 °C. The second part is an unsealed beaker with a diameter of 12 cm. At the start of the experiment, the reaction solution (volume, 300 ml) containing reactants and photocatalyst was put in the unsealed beakers, and a magnetic stirring device was used to stir the reaction solution. The distance between the light source and the surface of the reaction solution is 11 cm. In the experiments, the initial pH of the reaction solution is 5.0. The illumination time is 60 min, and the amount of the photocatalyst used is 2.0 g/l. The initial concentrations of MB and BF are 0.9×10^{-5} mol/l and 1.0×10^{-5} mol/l, respectively. In order to disperse the photocatalyst powder, the suspensions were ultrasonically vibrated for 20 min prior to irradiation. After the illumination, the samples (volume of each was 5 ml) taken from the reaction suspension were centrifuged at 7000 rpm for 20 min and filtered through a 0.2 μm millipore filter to remove the particles. The filtrate was then analyzed. In order to determine the reproducibility of the results, at least duplicated runs were carried out for each condition for averaging the results, and the experimental error was found to be within ± 4%.

2.4. Characterization

In order to determine the crystal phase composition and the crystallite size of the photocatalysts, XRD measurement was carried out at room temperature using a Bruker D8 advance X-ray powder diffractometer with Cu Kα radiation and a scanning speed of 3°/min. The accelerating voltage and emission current were 40 kV and 30 mA, respectively. The crystallite size was calculated by X-ray line broadening analysis using the Scherrer equation. TEM and high-resolution transmission electron microscopy (HR-TEM) images were performed with a JEOL-2010 transmission electron microscope, using an accelerating voltage of 200 kV. DRS measurements were carried out using a Hitachi UV-365 spectrophotometer equipped with an integrating sphere attachment. The analysis range was from 300 to 700 nm, and $BaSO_4$ was used as a reflectance standard. PL emission spectra were recorded on a JASCO FP-6500

type fluorescence spectrophotometer over a wavelength range of 350–600 nm. ESR signals of spin-trapped paramagnetic species with 5,5-dimethyl-l-pyrroline N-oxide (DMPO) were recorded with a Bruker A300E spectrometer. DMPO/H_2O and DMPO/CH_3OH were prepared by the conventional method. The experimental process is as follows: 10 mg samples and 40 μl DMPO were dissolved in 0.5 ml deionized water and stirred for 5 min, assigned as solution A. 10 mg samples and 40 μl DMPO were dissolved in 0.5 ml CH_3OH and stirred for 5 min, assigned as solution B. Solution A was used as the detection of hydroxyl radicals (DMPO-$^{\bullet}OH$), and solution B was used as the detection of superoxide radicals (DMPO-$^{\bullet}O_2^-$). The Brunauer–Emmett–Teller (BET) surface areas were measured using a Micromeritics ASAP 2020 N_2–physisorption method at 77 K.

2.5. Analysis

The concentrations of MB and BF in solution were determined by spectrophotometer. The photocatalytic efficiencies of MB and BF were calculated from the following expression:

$$\eta = \left[\frac{(C_0 - C_t)}{C_0}\right] \times 100\% \quad (1)$$

where η is the photocatalytic efficiency; C_0 is the concentration of reactant before illumination; C_t is the concentration of reactant after illumination time t.

3. Results and discussion

3.1. Characterization of WO_3(wt.%)/C_3N_4 photocatalyst

3.1.1. XRD analysis

Fig. 1a shows the XRD patterns of pure g-C_3N_4 and WO_3/g-C_3N_4, and Fig. 1b shows the XRD patterns of WO_3 and g-C_3N_4/WO_3. From Fig. 1a, it is clear that g-C_3N_4 shows two basic diffraction peaks at around 27.8° and 13.3°, which can be indexed as (0 0 2) and (1 0 0) diffraction planes (JCPDS 87-1526). The former, which corresponds to the interlayer distance of 0.325 nm, is attributed to the long-range interplanar stacking of aromatic systems; the latter with a much weaker intensity, which corresponds to a distance d = 0.676 nm, is related to an in-plane structural packing motif. The two diffraction peaks are in good agreement with the reported results of g-C_3N_4 [19–21]. The crystal structure of WO_3 is shown in Fig 1b pattern (g). It can be seen that the XRD characteristic peaks of WO_3 are in high agreement with the standard monoclinic phase WO_3 according to XRD JCPDS card (No. 20-1324).

Form Fig. 1a, it can be found that the intensities of diffraction peaks of g-C_3N_4 become weaker with the increase in the contents of WO_3 gradually. When the amount of WO_3 is lower than 7.0 wt.%, the characteristic peaks of WO_3 cannot be found. It is suggested that WO_3 may be highly dispersed on the surface of g-C_3N_4. However, from Fig. 1a and b, it is clear that when the amount WO_3 is higher than 10 wt.%, the characteristic peaks of g-C_3N_4 do not occur in the XRD pattern. It means that g-C_3N_4 is fully covered by WO_3 powder. It is notable that when WO_3 is coupled with g-C_3N_4, the characteristic peaks of g-C_3N_4 are weakened and the (0 0 2) peak of g-C_3N_4 is shifted from 27.8 to 28.4. Compared with the patterns g and h in Fig. 1a, when the amount WO_3 is 7.0 wt.%, the characteristic peaks of WO_3 in pattern f are also shifted to higher diffraction angle for 0.5. Meanwhile, it can also be seen that from Fig. 1b, when g-C_3N_4 is coupled with WO_3, compared with the XRD pattern of pure WO_3, the characteristic peaks of WO_3 in the composite g-C_3N_4/WO_3 are shifted to smaller diffraction angle for 0.6. Based on the results, it is proposed that the coupling between g-C_3N_4 and WO_3 may happen on the g-C_3N_4-{0 0 2} facets [33]. After facet coupling between g-C_3N_4 and WO_3, the g-C_3N_4-{0 0 2} facets are covered by WO_3, so the intensities of diffraction peaks of g-C_3N_4 should be decreased.

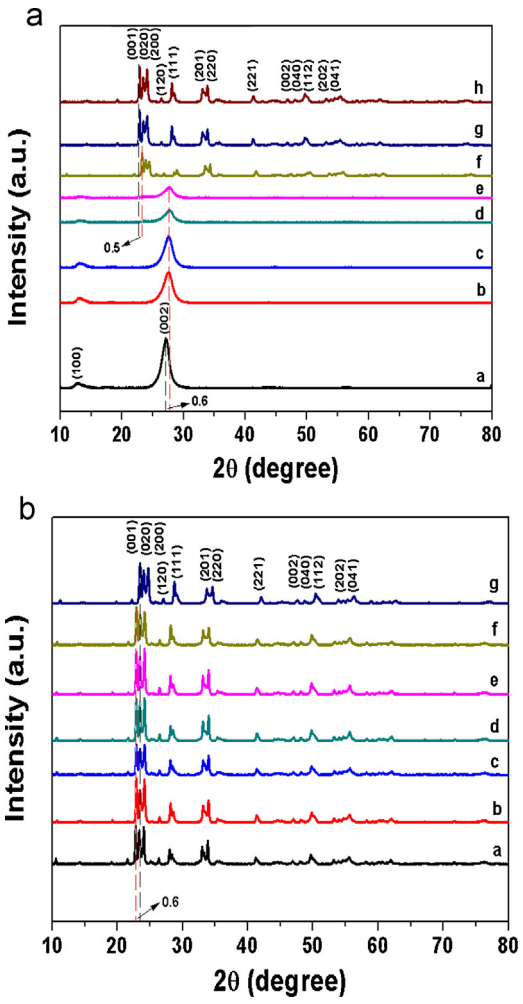

Fig. 1. a. XRD patterns of g-C_3N_4 and WO_3(wt.%)/g-C_3N_4 photocatalysts. a: g-C_3N_4, b: WO_3(1.0 wt.%)/g-C_3N_4, c: WO_3(3.0 wt.%)/g-C_3N_4, d: WO_3(5.0 wt.%)/g-C_3N_4, e: WO_3(7.0 wt.%)/g-C_3N_4, f: WO_3(10 wt.%)/g-C_3N_4, g: WO_3(30 wt.%)/g-C_3N_4, h: WO_3(50 wt.%)/g-C_3N_4
b. XRD patterns of WO_3(wt.%)/g-C_3N_4 and WO_3 photocatalysts. a: WO_3(70 wt.%)/g-C_3N_4, b: WO_3(90 wt.%)/g-C_3N_4, c: WO_3(93 wt.%)/g-C_3N_4, d: WO_3(95 wt.%)/g-C_3N_4, e: WO_3(97 wt.%)/g-C_3N_4, f: WO_3(99 wt.%)/g-C_3N_4, g: WO_3

When the amount of WO_3 is higher than 10 wt.%, the surface of g-C_3N_4 is fully covered by WO_3 powder. Meanwhile, strong interreaction between g-C_3N_4 and WO_3 results in the shift of characteristic peaks of g-C_3N_4 and WO_3, respectively.

3.1.2. UV–vis absorption spectra

The UV–vis absorption spectra of g-C_3N_4, WO_3(wt.%)/C_3N_4 and WO_3 photocatalysts are shown in Fig. 2a and b. It is known that the optical absorption of a semiconductor is closely related to its electronic structure. It is clear that from Fig. 2a, the g-C_3N_4 sample shows absorption wavelengths from the UV to the visible range up to 460 nm, which can be assigned to the intrinsic band gap of g-C_3N_4 (2.7 eV). Compared with pure g-C_3N_4, the absorption wavelength region of WO_3(wt.%)/C_3N_4 is extended toward visible light region, and stronger absorption in the visible region at wavelengths longer than 400 nm is observed. At the same time, the red shift and absorbance are enhanced with the increase in the amount of WO_3, which subsequently results in the efficient utilization of visible light. The above results may be attributed to the interaction between the g-C_3N_4 and WO_3 in the composite samples [22,25,26,34]. Furthermore, when the amounts of WO_3 are 1.0 and 3.0 wt.%, the absorption spectra are almost the same. The same

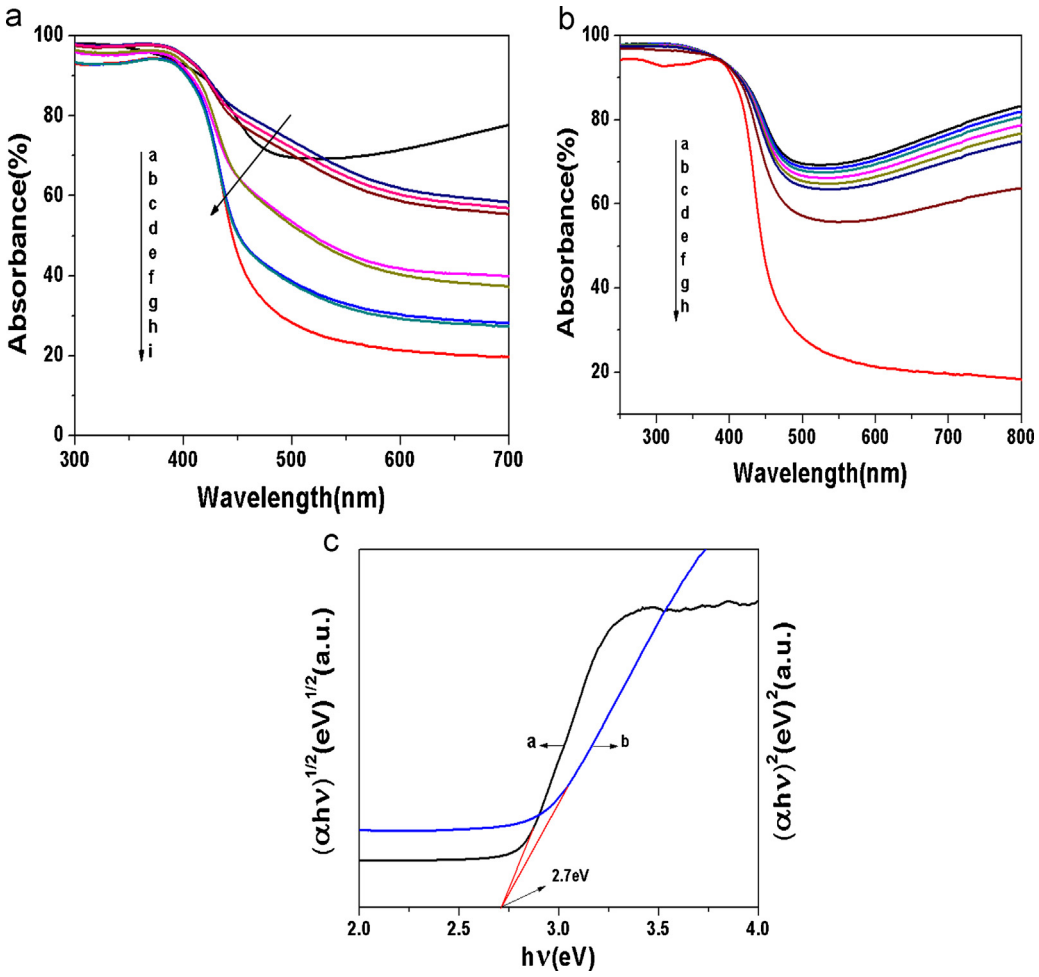

Fig. 2. a UV–vis absorption spectra of g-C_3N_4,WO_3(wt.%)/C_3N_4 and WO_3.
a: WO_3(10 wt.%)/g-C_3N_4, b: WO_3(30 wt.%)/g-C_3N_4, c: WO_3(50 wt.%)/g-C_3N_4, d: WO_3, e: WO_3(7.0 wt.%)/g-C_3N_4, f:WO_3(5.0 wt.%)/g-C_3N_4, g: WO_3(3.0 wt.%)/g-C_3N_4, h: WO_3(1.0 wt.%)/g-C_3N_4, i: g-C_3N_4
b. UV–vis absorption spectra of g-C_3N_4, WO_3(wt.%)/C_3N_4 and WO_3.
a: WO_3, b: WO_3(99 wt.%)/g-C_3N_4, c: WO_3(97 wt.%)/g-C_3N_4, d: WO_3(95 wt.%)/g-C_3N_4, e: WO_3(93 wt.%)/g-C_3N_4, f: WO_3(90 wt.%)/g-C_3N_4, g: WO_3(70 wt.%)/g-C_3N_4, h: g-C_3N_4 gr2
c. Band gap energies of g-C_3N_4(a) and WO_3(b).

results are obtained when the amounts of WO_3 are 5.0, 7.0, 10, 30, and 50 wt.%, respectively.

From Fig. 2b, it is clear that the absorption spectra of g-C_3N_4/WO_3 samples are attributed to that of WO_3. The absorption spectrum of g-C_3N_4/WO_3 falls in between g-C_3N_4 and WO_3 absorption spectra.

From Fig. 2a and b, it can also be seen that the absorption spectra of WO_3 showed a strong absorption tail at the wavelength longer than 500 nm. It is attributed to the hue of WO_3 powder which is markedly darker than the hue of C_3N_4 powder. At the same time, W^{5+} species appear on the surfaces of the WO_3, which has strong absorption ability in the visible light range [35,36].

It is known that the band gap energy of the photocatalysts can be calculated by the following equation:

$$\alpha h\nu = A(h\nu - E_g)^{n/2} \quad (2)$$

In this equation, α, h, v, A, and E_g are absorption coefficient, Planck constant, light frequency, proportionality and band gap energy, respectively; n keys the properties of the transition in a semiconductor ($n = 1$ for direct transition, and $n = 4$ for indirect transition). The values of n for g-C_3N_4 and WO_3 are 4 and 1, respectively [20,22,27]. By applying this equation, the band gaps of g-C_3N_4 and WO_3 are all 2.7 eV (See Fig. 2c), which agrees with the previous reports [20,26,28,29].

The band edge positions of CB and VB of semiconductor can be determined by a simple approach [31,32]. The valance band edge (E_{VB}) and conduction band edge (E_{CB}) of a semiconductor at the point of zero charge (pH_{ZPC}) can be predicted by the following equation:

$$E_{VB} = X - E_e + 0.5E_g \quad (3)$$

$$E_{CB} = E_{VB} - E_g \quad (4)$$

where X is the absolute electronegativity of the semiconductor, expressed as the geometric mean of the absolute electronegativity of the constituent atoms, which is defined as the arithmetic mean of the atomic electron affinity and the first ionization energy; E_e is the energy of free electrons on the hydrogen scale (likely 4.5 eV), and E_g is the band gap energy of the semiconductor. The X values for g-C_3N_4 and WO_3 are 4.73 and 6.49 eV, respectively. The E_{CB} of g-C_3N_4 and WO_3 are calculated to be −1.12 and 0.74 eV, respectively; and the E_{VB} of g-C_3N_4 and WO_3 are estimated to be 1.58 and 3.44 eV, respectively. The results are in accordance with the reported results [18,26,37].

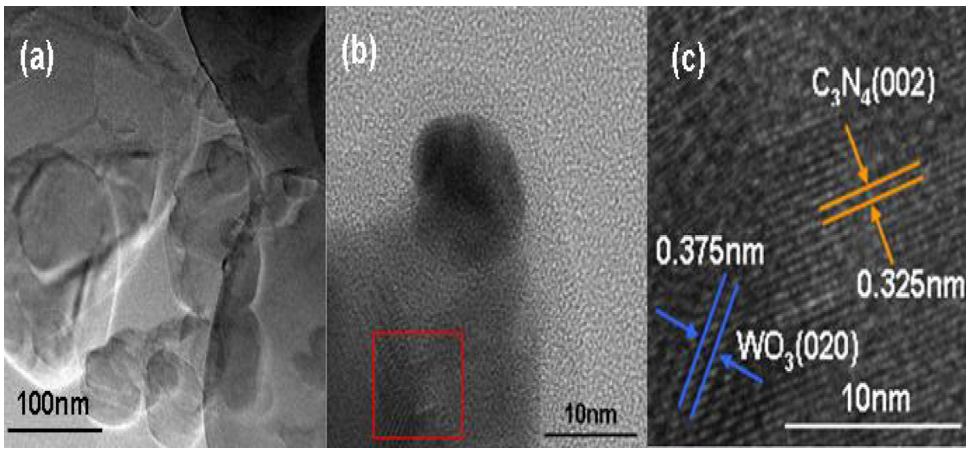

Fig. 3. TEM and HR-TEM images of WO_3/g-C_3N_4 photocatalyst.

3.1.3. TEM analysis

TEM was used to investigate the morphology and microstructure of the sample. Fig. 3 shows the TEM and HR-TEM images of WO_3(5.0 wt.%)/C_3N_4. It can be seen that WO_3 particles are uniformly deposited on the surface of g-C_3N_4. HR-TEM shows the existence of heterojunction between g-C_3N_4 and WO_3. It is clear that g-C_3N_4 and WO_3 display different orientations and lattice spacing. Two different kinds of lattice fringes are clearly observed. One fringe with d = 0.375 nm matches the (0 2 0) crystallographic plane of WO_3, and the other of d = 0.325 nm is attributed to the (0 0 2) crystallographic plane of g-C_3N_4. Therefore, an integration interface between g-C_3N_4-{0 0 2} and WO_3-{0 2 0} is formed, which is favorable for the transport of photoexcited carriers.

3.2. Photocatalytic properties of WO_3(wt.%)/g-C_3N_4

The photocatalytic activity of WO_3(wt.%)/g-C_3N_4 was evaluated by degradation of MB and BF. The photocatalytic degradation of MB and BF with different photocatalysts in the dark could be negligible under the consistent experimental conditions. At the same time, the dark absorption test in the absence of irradiation but with the catalysts shows that no significant change in the substrate concentration is found. For comparison, the photocatalytic properties of pure g-C_3N_4 and WO_3 were also tested under identical experimental conditions. The results are shown in Fig. 4a and b.

From Fig. 4a and b, it is clear that the photocalytic activities of pure g-C_3N_4 and WO_3 can be easily found. The photocatalytic efficiencies of g-C_3N_4 for MB and BF are 35.6% and 30.9%, respectively, and the photocatalytic efficiencies of pure WO_3 for MB and BF are 40.0% and 42.4%, respectively. For the WO_3/g-C_3N_4 photocatalyst, it is obvious that the photocatalytic activity increases greatly with the increase in the amount of WO_3. When the amount of WO_3 is 5.0 wt.%, the photocatalyst exhibits the best photocatalytic activity, the photocatalytic efficiencies for MB and BF are 87.9% and 75.6%, respectively. However, when the amount of WO_3 is higher than 5.0 wt.%, the photocatalytic activity of the photocatalyst decreases gradually. Compared with the pure g-C_3N_4 and WO_3, the WO_3/g-C_3N_4 photocatalyst performs excellent photocatalytic activity. It is clear that the photocatalytic activity of the photocatalysts decreases as follows: WO_3(5.0 wt.%)/g-C_3N_4 > WO_3(3.0 wt.%)/g-C_3N_4 > WO_3(7.0 wt.%)/g-C_3N_4 > WO_3(10 wt.%)/g-C_3N_4 > WO_3(1.0 wt.%)/g-C_3N_4 > g-C_3N_4. However, for the g-C_3N_4/WO_3 photocatalyst, the photocatalytic activity is improved slightly compared with pure WO_3. When the percentage of WO_3 is between 90 and 99, the photocalytic activities of g-C_3N_4/WO_3 photocatalysts are almost the same.

Based on the results, it is clear that the amount of WO_3 has an important effect on the photocatalytic activity of the WO_3/g-C_3N_4 photocatalyst. However, the amount of g-C_3N_4 has no obvious influence on the photocatalytic activity of the g-C_3N_4/WO_3 photocatalysts. The reason may be attributed to the different separation

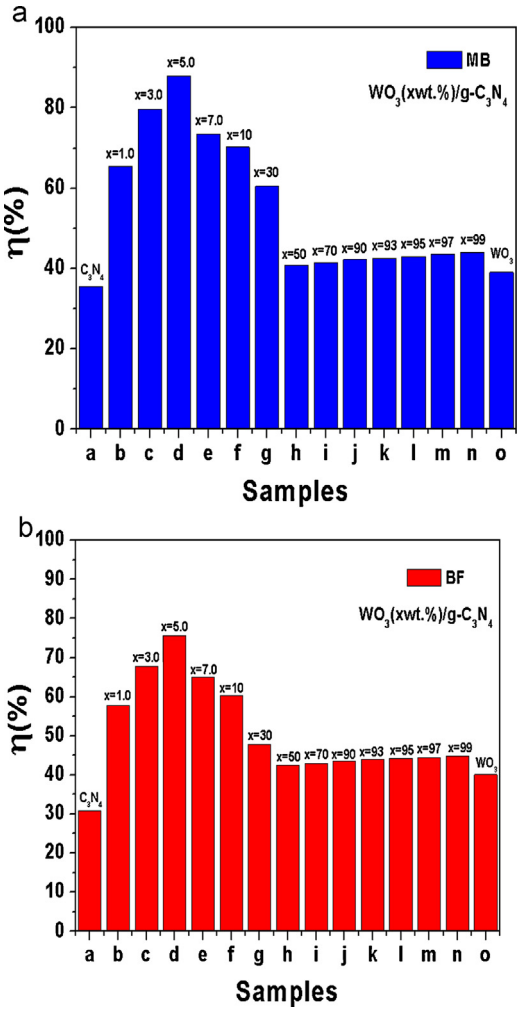

Fig. 4. a. The degradation of MB with different photocatalysts under visible light irradiation.
b. The degradation of BF with different photocatalysts under visible light irradiation.

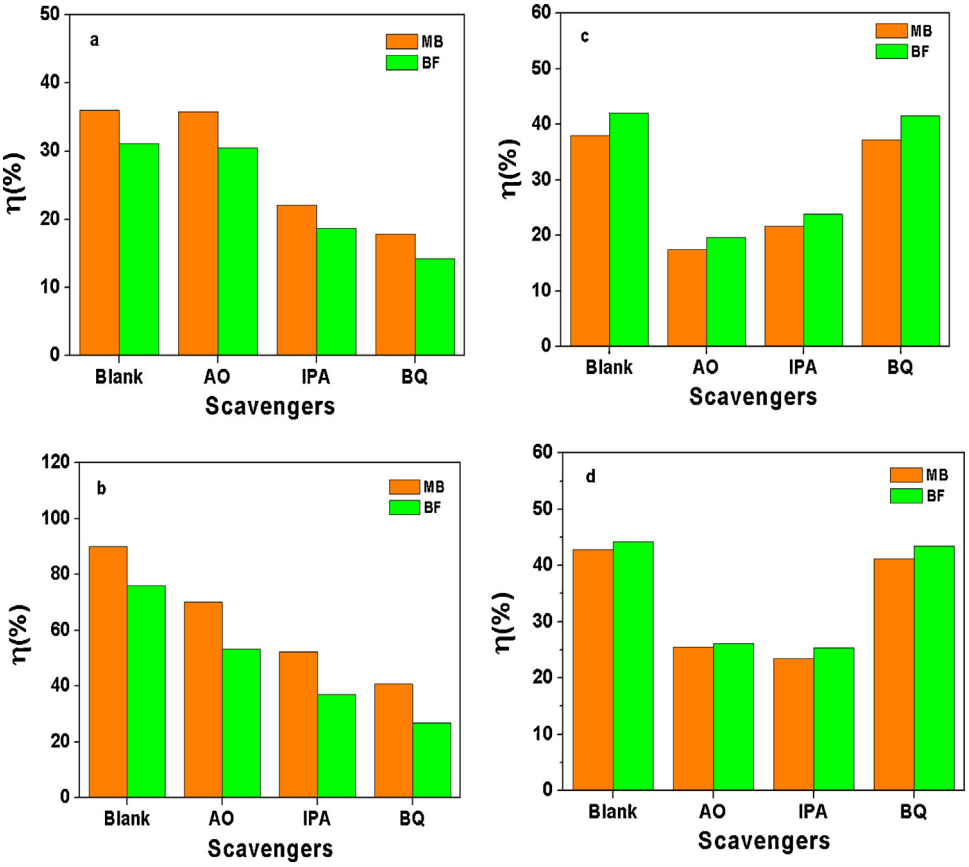

Fig. 5. Effects of a series of scavengers on the photocatalytic efficiency of samples. (a) g-C_3N_4, (b) WO_3(5.0 wt.%)/g-C_3N_4, (c)WO_3, (d) WO_3(95 wt.%)/g-C_3N_4 (The dosage of scavengers = 0.1 mmol/l, Illumination time t = 60 min)

mechanisms of the photoexcited carriers for photocatalysts with the different main parts.

The BET surface areas of the WO_3(wt.%)/g-C_3N_4 are 10.2, 10.2, 9.3, 9.6, 9.2, and 8.7 m^2/g for the samples with the wt.% value of 0, 1.0, 3.0, 5.0, 7.0 and 10, respectively. It is clear that the BET surface areas of the samples are slightly decreased with the increase in the amount of WO_3. Obviously, the enhancement of photocatalytic activities cannot be attributed to the BET surface area of the samples. Therefore, the enhanced photocatalytic activity of the samples can only be ascribed to the presence of WO_3. For the g-C_3N_4/WO_3 photocatalysts, the BET surface areas of the g-C_3N_4/WO_3(wt.%) are 5.9, 5.9, 5.6, 5.3, 5.3, and 4.9 m^2/g for the samples with the wt.% value of 90, 93, 95, 97, 99, and 100, respectively. So, the photocatalytic activity of g-C_3N_4/WO_3 has no direct relation with the BET surface areas.

In order to verify the complete degradation of MB in the reaction system, the generated gases in the reaction process were collected and passed into the aqueous solution of calcium hydroxide. The result showed that the solution of calcium hydroxide can be changed into turbidity, suggesting CO_2 was produced in the reaction system. So, it is proposed that MB dye can be degraded completely in the system.

Furthermore, in order to determine the photocatalytic activity of the photocatalyst for organic compounds which have no absorption in visible region, monocrotophos (an organophosphorus pesticide) was selected as a probe molecule of organic pollutants. It is known that PO_4^{3-} is one of the final degradation products of monocrotophos. Its formation rate can indicate the rate of complete degradation of monocrotophos[38]. The results showed that composite photocatalyst WO_3(5.0 wt.%)/g-C_3N_4 exhibited a much higher photocatalytic activity for the photocatalytic degradation of monocrotophos under visible light illumination. Under illumination for 30 min, 67.3% of monocrotophos (1.0×10^{-4} mol/l) can be degraded into PO_4^{3-}.

3.3. Reaction mechanisms of the g-C_3N_4-WO_3 photocatalysts

3.3.1. Determination of the reactive species

It has been reported that the $^{\bullet}O_2^-$, h^+, and $^{\bullet}OH$ are the major reactive species for the photocatalytic oxidation. In order to investigate the photocatalytic mechanisms of the WO_3-g-C_3N_4 photocatalyst, several scavengers were used to explore the reactive species in the process of photocatalytic reaction. Adding different scavengers into reaction solutions to remove the corresponding reactive species, the functions of different reactive species in the photocatalytic process based on the change of photocatalytic efficiency could be made clear. In the paper, the ammonium oxalate (AO) was used to remove hole (h^+). Isopropanol (IPA) was employed to impair the hydroxyl radical ($^{\bullet}OH$), and the benzoquinone (BQ) was applied to reduce the superoxide radical ($^{\bullet}O_2^-$) [39–42]. The results are shown in Fig. 5.

Fig. 5(a) shows the photocatalytic efficiencies of MB and BF with g-C_3N_4 photocatalyst in the conditions of adding various scavengers. It is known that the photocatalytic efficiencies of MB and BF are 35.6% and 30.9% without scavengers, respectively. When the AO was added into reaction solution, the photocatalytic efficiency is almost invariable. Therefore, hole is not the major reactive species. However, when the IPA was added into reaction solution, the degradation efficiencies of MB and BF decrease to 22.1% and 18.7%, respectively. When BQ was added into reaction solution, the

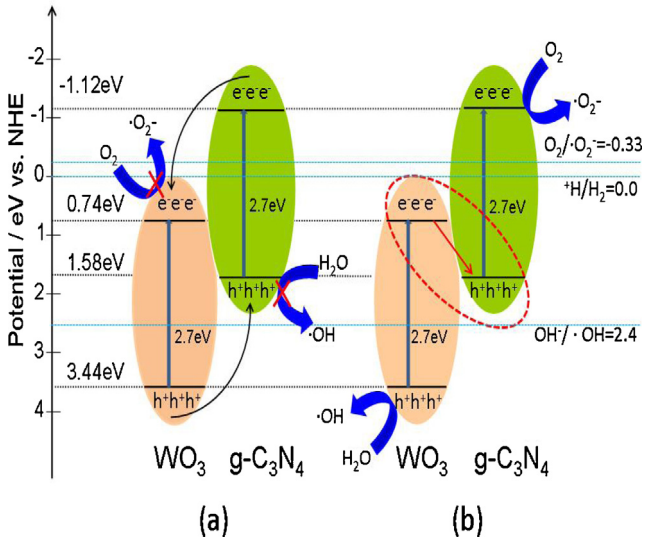

Fig. 6. Schematic diagram of photoexcited electron-hole separation process.

photocatalytic efficiencies are whittled down into 17.9% and 14.3%, respectively. Based on the results, it is clear that $^{\bullet}O_2^-$ and •OH are the major reactive species in the photocatalytic reaction system for pure g-C_3N_4 photocatalyst.

For the WO_3(5.0 wt.%)/g-C_3N_4 photocatalyst, the effects of various scavengers on the photocatalytic efficiencies of MB and BF are shown in Fig. 5(b). The degradation efficiencies of MB and BF are 87.9% and 75.6% respectively when no scavenger was added. When the AO was added into reaction solution, the degradation efficiencies of MB and BF are decreased to 70.1% and 53.5%, respectively. When IPA was added into the reaction solutions, the degradation efficiencies of MB and BF decrease to 52.4% and 37%, respectively. When adding BQ into the reactions, the degradation efficiencies of MB and BF are whittled down into 40.7% and 26.9%, respectively. It is clear that h^+, •OH, and $^{\bullet}O_2^-$ are the major reactive species for the WO_3(5.0 wt.%)/g-C_3N_4 photocatalyst. The influencing degree is $^{\bullet}O_2^- > {}^{\bullet}OH > h^+$.

For the pure WO_3 photocatalyst as shown in Fig. 5(c), the degradation efficiencies of MB and BF are 40% and 42.4% when no scavenger was added. When adding BQ into reaction solution, the photocatalytic efficiency is not changed. However, when adding the AO and IPA into the reaction system respectively, the degradation efficiencies of MB and BF are decreased greatly. Obviously, the major reactive species for pure WO_3 are h^+ and •OH.

It is clear in Fig. 5(d) that the photocatalytic efficiencies of MB and BF for the WO_3(95 wt.%)/g-C_3N_4 photocatalyst are 43% and 44.2% without scavengers, respectively. When the BQ was added into reaction solution, the photocatalytic efficiency is not obviously changed. When adding the AO and IPA into the reaction systems respectively, the degradation efficiencies of MB and BF are decreased greatly. But the influencing extent is lower than that of WO_3. It is obvious that the conclusion is the same as that of pure WO_3. Namely, h^+ and •OH are the major reactive species in the photocatalytic reaction system for the WO_3(95 wt.%)/g-C_3N_4 photocatalyst.

3.3.2. *Proposed mechanisms of the g-C_3N_4-WO_3 photocatalyst*

It is known that, when WO_3 and g-C_3N_4 are coupled, a heterojunction photocatalyst between WO_3 and g-C_3N_4 will be formed. According to the band gap structures of WO_3 and g-C_3N_4, the separation processes of photoexcited electron-hole can be described in Fig. 6(a) and (b), respectively. If the charge carriers of WO_3-g-C_3N_4 photocatalyst transfer according to Fig. 6(a), which is the generic electron-hole separation process for a great number of composite photocatalysts; the electrons in the CB of g-C_3N_4 will migrate to the CB of WO_3, and holes in the VB of WO_3 will migrate to the VB of g-C_3N_4. As a result, these accumulated electrons in the CB of WO_3 can not reduce O_2 to yield $^{\bullet}O_2^-$, and the holes in the VB of g-C_3N_4 can not oxidize OH to give •OH. Therefore, when the charge carriers of the photocatalyst transfer in accordance with the traditional model, it is not favorable for the formation of active species, and leads to lower photocatalytic activity of reaction system. However, if the charge carriers of WO_3-g-C_3N_4 photocatalyst transfer according to Fig. 6 (b), which is a direct Z-scheme photocatalyst, the fast combination is achieved between the photoexcited electrons in the CB of WO_3 and photoexcited holes in the VB of g-C_3N_4. At the same time, the electrons in the CB of g-C_3N_4, which have more negative potential, reduce the molecular oxygen to yield $^{\bullet}O_2^-$; and the holes in the VB of WO_3, which have more positive potential, generate abundant active •OH radicals. Namely, a typical Z-scheme photocatalyst is favorable for the production of $^{\bullet}O_2^-$ and •OH reactive species.

Based on the results of photocatalytic activity and the reactive species of the g-C_3N_4-WO_3 reaction systems, it is known that, for the g-C_3N_4/WO_3 photocatalyst, h^+ and •OH are the major reactive species, which are the same as those of pure WO_3. Furthermore, the photocatalytic activity is not obviously increased compared with pure WO_3. The reason may be that when the amount of WO_3 is higher than 10.0 wt.%, the surface of g-C_3N_4 is covered by WO_3 powder entirely (see XRD patterns), and the role of g-C_3N_4 is not played fully. So, it exhibits similar properties with WO_3. Meanwhile, only a small amount of g-C_3N_4 is coupled with WO_3 forming heterojunctions. Based on the result of PL emission spectra (See Fig. 9b), it is suggested that Fig. 6(a) shows the separation process of photoexcited electron-hole pairs for the g-C_3N_4/WO_3 photocatalysts. However, for the WO_3/g-C_3N_4 photocatalytic system in the experimental conditions, the $^{\bullet}O_2^-$, •OH, and h^+ are the major reactive species, and the photocatalyst exhibits higher photocatalytic activity. So the separation process of the photoexcited electron-hole pairs should be confirmed according to Fig. 6(b). In this way, the photocatalytic activity of the WO_3/g-C_3N_4 system is significantly increased, and FB or MB is decomposed by •OH, $^{\bullet}O_2^-$ or direct h^+ reactive species.

Based on the analysis, it is proposed that Fig. 6(a) is the separation process of photogenerated electron-hole pairs for the g-C_3N_4/WO_3 photocatalyst, and the WO_3/g-C_3N_4 is a typical Z-scheme photocatalyst. The transport process of photogenerated electron-hole pairs is in accordance with Fig. 6(b) under our experimental conditions.

3.3.3. *Evidences of the mechanism*

3.3.3.1. ESR analysis. In order to determine the correctness of the mechanism, the production of $^{\bullet}O_2^-$ and OH radicals in the reaction systems was detected by the ESR technique [43–45]. The result is shown in Fig. 7.

Fig. 7a shows the ESR signals of DMPO-$^{\bullet}O_2^-$ for g-C_3N_4, WO_3(5.0 wt.%)/g-C_3N_4, WO_3(95 wt.%)/g-C_3N_4, and WO_3, respectively. For the curves of g-C_3N_4 and WO_3(5.0 wt.%)/g-C_3N_4, the six characteristic peaks of the DMPO-$^{\bullet}O_2^-$ adducts are observed. It is obvious that $^{\bullet}O_2^-$ radicals are generated on the two samples after irradiation. It's worth noting that the intensity of peaks of WO_3(5.0 wt.%)/g-C_3N_4 is stronger than that of g-C_3N_4. That is to say, the amount of $^{\bullet}O_2^-$ radicals generated on the WO_3(5.0 wt.%)/g-C_3N_4 surface is more than that of g-C_3N_4. However, for the WO_3(95 wt.%)/g-C_3N_4 and WO_3 photocatalysts, there is no characteristic peak of DMPO-$^{\bullet}O_2^-$. It means that few $^{\bullet}O_2^-$ radicals are generated on the surface of the samples.

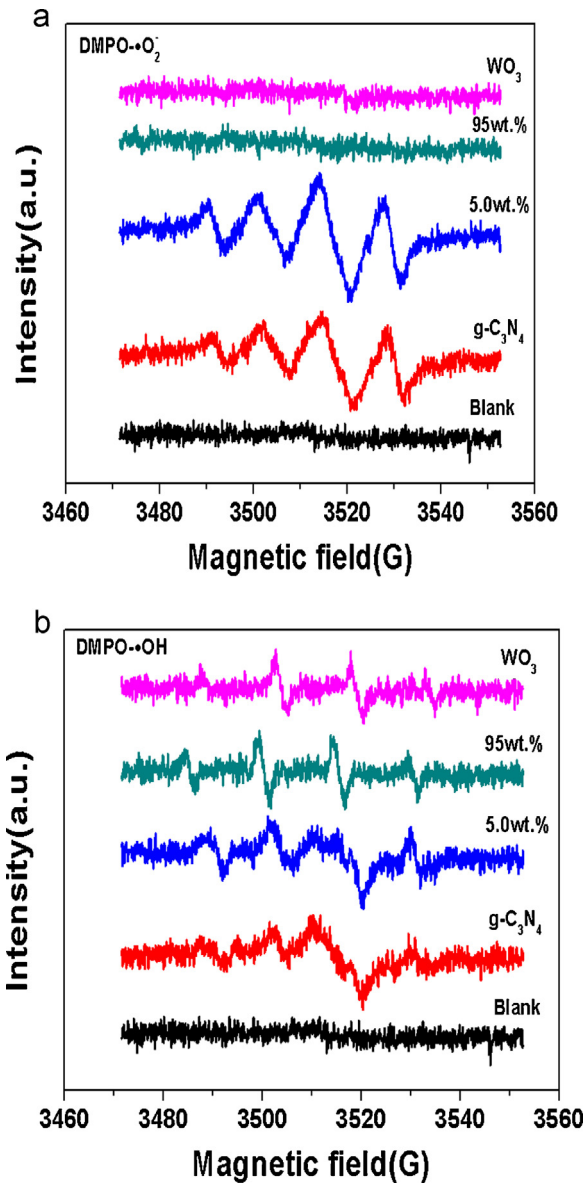

Fig. 7. a. ESR signals of the DMPO-•O_2^- with irradiation for 20 s in methanol dispersion.b. ESR signals of the DMPO-•OH with irradiation for 20 s in aqueous dispersion.

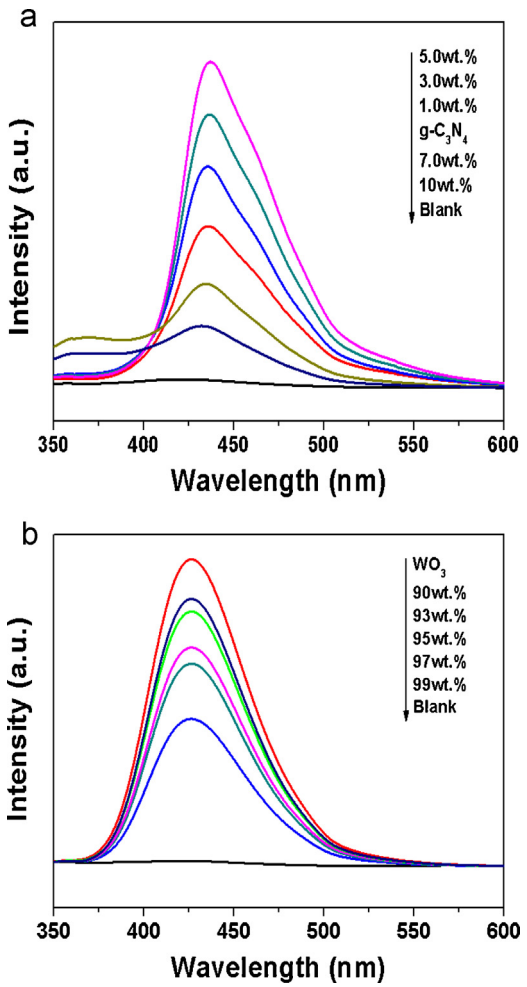

Fig. 8. a. The PL intensity of g-C_3N_4 and WO_3(wt.%)/g-C_3N_4 in TA solution under visible light irradiation. (x = 1.0, 3.0, 5.0, 7.0, 10).b. The PL intensity of WO_3 and WO_3(wt.%)/g-C_3N_4 in TA solution under visible light irradiation (x = 90, 93, 95, 97, 99).

From Fig. 7b, it is clear that four characteristic peaks of DMPO-•OH could be observed in the curves of g-C_3N_4, WO_3(5.0 wt.%)/g-C_3N_4, WO_3(95 wt.%)/g-C_3N_4, and WO_3. There was no DMPO-•OH adducts in dark conditions. It is demonstrated that •OH radicals were generated on the four samples after illumination. However, it is difficult to determine the intensity of peaks of the samples.

Hydroxyl radicals (•OH) generated on the surface of different photocatalysts were also detected by the fluorescence spectrometer with a 5×10^{-4} mol/l basic solution of terephthalic acid (TA) [32,39,43]. TA readily reacts with •OH to produce a highly fluorescent product, i.e., 2-hydroxyterephthalic acid, whose PL peak intensity is in proportion to the amount of •OH radicals formed in water. The experimental procedures were reported in the earlier reports [31,32,39]. The fixed illumination time is 60 min.

Fig. 8a shows the PL spectra of WO_3/g-C_3N_4 photocatalysts. It is clear that the generation rate of •OH radicals on the WO_3(5.0 wt.%)/g-C_3N_4 surface is higher than those of other photocatalysts. When the content of WO_3 is lower than 5.0 wt.%, the generation rate of •OH radicals of WO_3(wt.%)/g-C_3N_4 is more than that of pure g-C_3N_4. However, when the amount of WO_3 is higher than 7.0 wt.%, the generation rate of •OH radicals is less than that of pure g-C_3N_4. The result is in accordance with the photocatalytic activities of the WO_3(wt.%)/g-C_3N_4 photocatalysts. Fig. 8b shows the PL spectra of g-C_3N_4/WO_3 photocatalysts. It can be seen that, the generation rate of •OH radicals on the WO_3 surface is higher than those of others, and with the increase in the content of WO_3, the generation rate of •OH radicals of g-C_3N_4/WO_3 is decreased gradually.

Based on the results of ESR and PL techniques, it is clear that the proposed reaction mechanism is reasonable. Namely, for the WO_3/g-C_3N_4 photocatalyst, the photoexcited carriers transfer according to Fig. 6(b); and for the g-C_3N_4/WO_3 photocatalyst, the separation process of photogenerated electron-hole pairs should be in accordance with Fig. 6(a). The difference of the main parts of the photocatalysts will result in different reactive species in the reaction system, and thereby affect the photocatalytic activity of the photocatalysts.

3.3.3.2. Photoluminescence emission spectra. The PL emission spectra were employed to investigate the combination and separation of the photoinduced carriers which played a crucial role in photocatalytic reactions. The intensity of PL emission spectra indicates the recombination speed of photoexcited electron-hole pairs. The stronger the PL intensity is the faster is

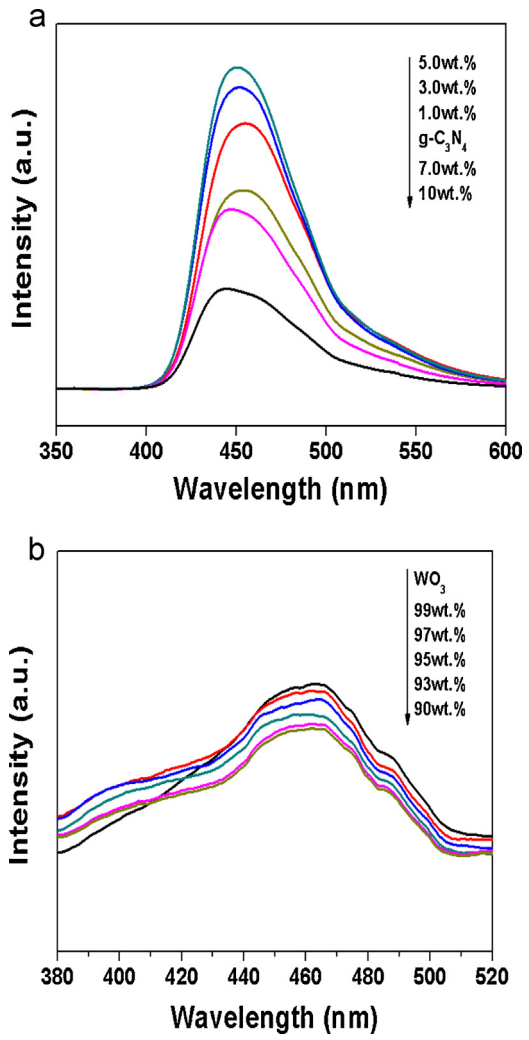

Fig. 9. a. Photoluminescence emission spectra of pure g-C_3N_4 and WO_3(*x*wt.%)/g-C_3N_4 samples (*x* = 1.0, 3.0, 5.0, 7.0, 10).
b. Photoluminescence emission spectra of pure WO_3 and WO_3(*x*wt.%)/g-C_3N_4 samples (*x* = 90, 93, 95, 97, 99).

the combination of the photoexcited electron-hole. Generally, a higher PL intensity indicates a higher recombination rate of photoexcited electron-hole, and a lower PL intensity expresses a lower recombination rate of photoexcited electron-hole [32,39,40].

Fig. 9a shows the PL spectra of the WO_3(wt.%)/g-C_3N_4 photocatalysts with wt.% of 1.0, 3.0, 5.0, 7.0, 10 and g-C_3N_4, respectively. It is clear that the PL spectra of the photocatalysts have a strong emission peak at around 450 nm, which could be related to the recombination of the photoexcited electron-hole of g-C_3N_4 [22,23,34]. From Fig. 9a, it can be seen that the PL intensity of the WO_3(5.0 wt.%)/g-C_3N_4 photocatalyst exhibits the strongest emission, suggesting that the recombination of the photoexcited electron-hole on the WO_3(5.0 wt.%)/g-C_3N_4 photocatalyst surface is the highest. The PL intensity decreases with the decrease of WO_3 from 5.0 wt.% to 0 wt.%. However, when the amount of WO_3 is higher than 5.0 wt.%, the PL intensities of WO_3/g-C_3N_4 photocatalysts are lower than that of pure g-C_3N_4 photocatalyst, which means that the recombination of the photoexcited electron-hole of WO_3/g-C_3N_4 photocatalysts is lower than pure g-C_3N_4. It indicates that, when the amount of WO_3 is higher than a certain amount (greater than 5.0 wt.%), the recombination of the photoexcited electron-hole is suppressed. The above results are consistent with the results of photocatalytic activity of the WO_3/g-C_3N_4 photocatalysts. It means that a higher PL intensity indicates a higher photocatalytic activity in the experimental conditions. In Fig. 9a, the higher PL intensities of the samples are attributed to the higher recombination rate between photoexcited electrons in the CB of WO_3 and photoexcited holes in the VB of g-C_3N_4, suggesting that rich electrons in the CB of g-C_3N_4 and holes in the VB of WO_3 participate in the reaction to produce $^{\bullet}O_2^-$ and $^{\bullet}OH$, respectively. So the photocatalytic activity is improved significantly. Based on the analysis, it is concluded that the WO_3(wt.%)/g-C_3N_4 system is a typical Z-scheme photocatalyst. At the same time, the PL spectra further demonstrate that the transport of photoexcited carriers of the WO_3(wt.%)/g-C_3N_4 is in accordance with the Fig. 6(b).

Fig. 9b shows the PL spectra of the g-C_3N_4/(wt.%)WO_3 photocatalysts with wt.% of 90, 93, 95, 97, 99 and pure WO_3. It is clear that the samples have a strong emission peak at around 460 nm, which could be related to the recombination of the photoexcited electron-hole of WO_3. The PL intensity of photocatalyst decreases gradually with the increase in the amount of g-C_3N_4, but the six curves are extremely adjacent. It is suggested that the recombination rate of photoexcited electron-hole of six samples is nearly the same. Namely, the separation rate of the photoexcited electron-hole pairs is nearly the same for the g-C_3N_4/WO_3 photocatalysts. Based on the results, it is concluded that when g-C_3N_4 is coupled with WO_3, the surface of g-C_3N_4 is covered by WO_3 powder, and the role of g-C_3N_4 is not played fully. Therefore, the photoexcited electron-hole pairs can not be separated effectively for the g-C_3N_4/WO_3 photocatalysts. The result is in accordance with the result of XRD. Based on the analysis, it is concluded that the g-C_3N_4/WO_3 photocatalyst is a generic band–band transfer photocatalyst. The PL spectra further demonstrate the transport of photoexcited electron-hole pairs of g-C_3N_4/WO_3 is in accordance with the Fig. 6(a).

4. Conclusions

The composite photocatalyst WO_3(wt.%)-g-C_3N_4 was fabricated via ball milling and heat treatment methods. The coupling between g-C_3N_4 and WO_3 may happen on the g-C_3N_4-{0 0 2} facets. When g-C_3N_4 is the major part of composite photocatalyst (namely WO_3/g-C_3N_4), the transfer of the photoexcited electrons and holes is according to the Z-scheme mechanism. In the system, the photoexcited holes in the VB of g-C_3N_4 and electrons in the CB of WO_3 are quickly combined. The accumulated electrons in the CB of g-C_3N_4 exhibit high reducibility to reduce the molecular oxygen to yield $^{\bullet}O_2^-$; and the holes in the VB of WO_3 display high oxidizability to oxidize H_2O or OH^- to generate abundant active $^{\bullet}OH$ radicals. So, the WO_3/g-C_3N_4 photocatalysts exhibit excellent photocatalytic activity. However, when WO_3 is the main part of the composite photocatalyst (namely g-C_3N_4/WO_3), the separation of the photogenerated electrons and holes adopts the band–band transfer. Meanwhile, the surface of g-C_3N_4 is covered by WO_3 powder, and the role of g-C_3N_4 is not played fully. So, the photocatalytic activity can not be enhanced greatly for the g-C_3N_4/WO_3 photocatalyst.

Acknowledgement

This study was supported by the Natural Science Foundation of China (NSFC, grant No. 20973071, 51172086, 51272081 and 21103060).

References

[1] G. Liu, P. Niu, C.H. Sun, S.C. Smith, Z.G. Chen, G.Q. Lu, H.M. Cheng, J. Am. Chem. Soc. 132 (2010) 11642–11648.
[2] Q. Xiang, J.G. Yu, M. Jaroniec, J. Am. Chem. Soc. 134 (2012) 6575–6578.
[3] J.D. Hong, X.Y. Xia, Y.S. Wang, R. Xu, J. Mater. Chem. 22 (2012) 15006–15012.

[4] N.S. Chaudhari, A.P. Bhirud, R.S. Sonawane, L.K. Nikam, S.S. Warule, V.H. Rane, B.B. Kale, Green Chem. 13 (2011) 2500–2506.
[5] L. Ge, C. Han, J. Liu, J. Mater. Chem. 22 (2012) 11843–11850.
[6] X.F. Chen, J.S. Zhang, X.Z. Fu, M. Antonietti, X.C. Wang, J. Am. Chem. Soc. 131 (2009) 11658–11659.
[7] X. Zong, G.P. Wu, H.J. Yan, G.J. Ma, J.Y. Shi, F.Y. Wen, L. Wang, C. Li, J. Phys. Chem. C 114 (2010) 1963–1968.
[8] F.Z. Jia, Z.P. Yao, Z.H. Jiang, Int. J. Hydrogen Energy 37 (2012) 3048–3055.
[9] M. Tabata, K. Maeda, M. Higashi, D. Lu, T. Takata, R. Abe, K. Domen, Langmuir 26 (2010) 9161–9165.
[10] P. Madhusudan, J.R. Ran, J. Zhang, J.G. Yu, G. Liu, Appl. Catal. B: Environ. 110 (2011) 286–295.
[11] L. Kong, Z. Jiang, H.H. Lai, R.J. Nicholls, T.C. Xiao, M.O. Jones, P.P. Edwards, J. Catal. 293 (2012) 116–125.
[12] M.T. Uddin, Y. Nicolas, C. Olivier, T. Toupance, L. Servant, M.M. Müller, H.J. Kleebe, J. Ziegler, W. Jaegermann, Inorg. Chem. 51 (2012) 7764–7773.
[13] L. Ye, J. Liu, C. Gong, L. Tian, T. Peng, L. Zan, J. Catal. 2 (2012) 1677–1683.
[14] J. Su, L. Guo, N. Bao, C.A. Grimes, Nano Lett. 11 (2011) 1928–1933.
[15] Z. Liu, Z.-G. Zhao, M. Miyauchi, J. Phys. Chem. C 113 (2009) 17132–17137.
[16] T. Li, L. Zhao, Y. He, J. Cai, M. Luo, J. Lin, Appl. Catal. B 129 (2013) 255–263.
[17] X.F. Wang, S.F. Li, Y.Q. Ma, H.G. Yu, J.G. Yu, J. Phys. Chem. C 115 (2011) 14648–14655.
[18] X.W. Wang, G. Liu, Z.G. Chen, F. Li, L.Z. Wang, G.Q. Lu, H.M. Cheng, Chem. Commun. (2009) 3452–3454.
[19] F. Dong, L.W. Wu, Y.J. Sun, M. Fu, Z.B. Wu, S.C. Lee, J. Mater. Chem. 21 (2011) 15171–15174.
[20] J.H. Liu, Y.W. Zhang, L.H. Lu, G. Wu, W. Chen, Chem. Commun. 48 (2012) 8826–8828.
[21] S.C. Yan, Z.S. Li, Z.G. Zou, Langmuir 25 (2009) 10397–10401.
[22] S.C. Yan, S.B. Lv, Z.S. Li, Z.G. Zou, Dalton Trans. 39 (2010) 1488–1491.
[23] Y.J. Wang, R. Shi, J. Lin, Y.F. Zhu, Energy Environ. Sci. 4 (2011) 2922–2929.
[24] L. Ge, F. Zuo, J.K. Liu, Q. Ma, C. Wang, D.Z. Sun, L.D. Bartels, P.Y. Feng, J. Phys. Chem. C 116 (2012) 13708–13714.
[25] L. Ge, C.C. Han, Appl. Catal. B: Environ. 117–118 (2012) 268–274.
[26] Y.J. Wang, X.J. Bai, C.S. Pan, J. He, Y.G. Zhu, J. Mater. Chem. 22 (2012) 11568–11573.
[27] A. Srinivasan, M. Miyauchi, J. Phys. Chem. C 116 (2012) 15421–15426.
[28] T. Nakajima, T. Kitamura, T. Tsuchiya, Appl. Catal. B: Environ. 108–109 (2011) 47–53.
[29] J. Kim, C.W. Lee, W. Choi, Environ. Sci. Technol. 44 (2010) 6849–6854.
[30] F.G. Wang, C.D. Valentin, G. Pacchioni, J. Phys. Chem. C 115 (2011) 8345–8353.
[31] S.F. Chen, Y.G. Yang, W. Liu, J. Hazard. Mater. 186 (2011) 1560–1567.
[32] S.F. Chen, M.S. Ji, W. Liu, Mater. Chem. Phys. 134 (2012) 951–957.
[33] L.Q. Ye, J.Y. Liu, Z. Jiang, T.Y. Peng, L. Zan, Appl. Catal. B: Environ. 142–143 (2013) 1–7.
[34] L. Ge, C.C. Han, J. Liu, Appl. Catal. B: Environ. 108–109 (2011) 100–107.
[35] W. Morales, M. Cason, O. Aina, N.R. de Tacconi, K. Rajeshwar, J. Am. Chem. Soc. 130 (2008) 6318–6319.
[36] M.S. Bazarjani, M. Hojamberdiev, Koji. Morita, G. Zhu, G. Cherkashinin, C. Fasel, T. Herrmann, H. Breitzke, A. Gurlo, R. Riedel, J. Am. Chem. Soc. 135 (2013) 4467–4475.
[37] Y. Xu, M.A.A. Schoonen, Am. Mineral. 85 (2000) 543–556.
[38] S.F. Chen, L. Chen, S. Gao, G.Y. Cao, Mater. Chem. Phys. 98 (2006) 116–120.
[39] J. Cao, B.D. Luo, H.L. Lin, B.Y. Xu, S.F. Chen, Appl. Catal. B: Environ. 111–112 (2012) 288–296.
[40] W.J. Li, D.Z. Li, Y.M. Lin, P.X. Wang, W. Chen, X.Z. Fu, Y. Shao, J. Phys. Chem. C 116 (2012) 3552–3560.
[41] Y.M. Lin, D.Z. Li, J.H. Hu, G.C. Xiao, J.X. Wang, W.J. Li, X.Z. Fu, J. Phys. Chem. C 116 (2012) 5764–5772.
[42] W.J. Wang, L.Z. Zhang, T.C. An, G.Y. Li, H.Y. Yip, P.K. Wong, Appl. Catal. B: Environ. 108–109 (2011) 108–116.
[43] M. Sun, D.Z. Li, W.J. Zhang, Z.X. Chen, H.J. Huang, W.J. Li, Y.H. He, X.Z. Fu, J. Solid State Chem. 190 (2012) 135–142.
[44] Y.B. Chen, D.Z. Li, M. He, Y. Hu, H. Ruan, Y.M. Lin, J.H. Hu, Y. Zheng, Y. Shao, Appl. Catal. B: Environ. 113–114 (2012) 134–140.
[45] M. Sun, D.Z. Li, Y. Zheng, W.J. Zhang, Y. Shao, Y.B. Chen, W.J. Li, X.Z. Fu, Environ. Sci. Technol. 43 (2009) 7877–7882.